

Temporal variation characteristics of cathode temperature in a magnetoplasmadynamic thruster

Cheng Zhou(周成), Peng Wu(吴鹏), Yun-Tao Song(宋云涛), Jin-Xing Zheng(郑金星), Yong Li(李永), Ge Wang(王戈), and Hai-Yang Liu(刘海洋)

Citation: Chin. Phys. B, 2025, 34 (**2**): 025202. DOI: 10.1088/1674-1056/ad9e9b
Journal homepage: http://cpb.iphy.ac.cn; http://iopscience.iop.org/cpb

What follows is a list of articles you may be interested in

Observation of Weibel magnetic fields in laser-produced interpenetrating flows

Chuanqi Shi(施川奇), Dawei Yuan(袁大伟), Wei Sun(孙伟), Yapeng Zhang(张雅芃), Zhijie Qiu(邱志杰), Huigang Wei(魏会冈), Zhe Zhang(张喆), Xiaohui Yuan(远晓辉), and Gang Zhao(赵刚)
Chin. Phys. B, 2025, 34 (**1**): 015203. DOI: 10.1088/1674-1056/ad94e4

Growth mechanism and characteristics of electron drift instability in Hall thruster with different propellant types

Long Chen(陈龙), Zi-Chen Kan(阚子晨), Wei-Fu Gao(高维富), Ping Duan(段萍), Jun-Yu Chen(陈俊宇), Cong-Qi Tan(檀聪琦), and Zuo-Jun Cui(崔作君)
Chin. Phys. B, 2024, 33 (**1**): 015203. DOI: 10.1088/1674-1056/acf9e5

Interaction between plasma and electromagnetic field in ion source of 10 cm ECR ion thruster

Hao Mou(牟浩), Yi-Zhou Jin(金逸舟), Juan Yang(杨涓), Xu Xia(夏旭), and Yu-Liang Fu(付瑜亮)
Chin. Phys. B, 2022, 31 (**7**): 075202. DOI: 10.1088/1674-1056/ac4906

Research of influence of the additional electrode on Hall thruster plume by particle-in-cell simulation

Xi-Feng Cao(曹希峰), Hui Liu(刘辉), Da-Ren Yu(于达仁)
Chin. Phys. B, 2020, 29 (**9**): 095204. DOI: 10.1088/1674-1056/aba2e3

The *E*×*B* drift instability in Hall thruster using 1D PIC/MCC simulation

Zahra Asadi, Mehdi Sharifian, Mojtaba Hashemzadeh, Mahmood Borhani Zarandi, Hamidreza Ghomi Marzdashti
Chin. Phys. B, 2020, 29 (**2**): 025204. DOI: 10.1088/1674-1056/ab6719

Temporal variation characteristics of cathode temperature in a magnetoplasmadynamic thruster

Cheng Zhou(周成)[1,2,3], Peng Wu(吴鹏)[3], Yun-Tao Song(宋云涛)[1,2], Jin-Xing Zheng(郑金星)[1,2], Yong Li(李永)[3,†], Ge Wang(王戈)[3], and Hai-Yang Liu(刘海洋)[2]

[1] *University of Science and Technology of China, Hefei* 230031, *China*
[2] *Hefei Institutes of Physical Science, Chinese Academy of Sciences, Hefei* 230031, *China*
[3] *Beijing Institute of Control Engineering, Beijing* 100080, *China*

(Received 7 October 2024; revised manuscript received 4 December 2024; accepted manuscript online 13 December 2024)

The magnetoplasmadynamic thruster (MPDT) is characterized by its high specific impulse and substantial thrust density, making it a promising propulsion system for deep space exploration missions. In both laboratory experiments and practical applications, cathode ablation has emerged as a critical concern. An optical diagnostic approach based on monochromatic radiation temperature measurement, utilizing plume emission spectra and the selection of an appropriate test band, has been successfully employed. This method provides an accurate temperature distribution across the cathode surface, offering a novel testing technique for the optimization and evaluation of magnetic plasma thruster designs.

Keywords: magnetoplasmadynamic thruster (MPDT), optical diagnostic, monochromatic radiation, cathode temperature

PACS: 52.75.Di, 85.70.Rp

DOI: 10.1088/1674-1056/ad9e9b **CSTR:** 32038.14.CPB.ad9e9b

1. Introduction

As space missions increasingly target destinations like the Moon, Mars, and other planets, there is a growing demand for thrusters with higher thrust capabilities. While traditional chemical propulsion systems provide the necessary thrust, electric propulsion offers a significant advantage in terms of higher specific impulse, allowing spacecraft to carry larger payloads. However, electric engines typically generate less than 1 N of thrust when operating at power levels below 10 kW.[1] To meet the demanding requirements of deep space missions, the power output of these thrusters must be scaled up to tens or even hundreds of kW. Among the potential high-power propulsion systems, the magnetoplasmadynamic thruster (MPDT) stands out for its compact and straightforward design, wide thrust range (1–100 N), high specific impulse (2000–5000 s), and impressive efficiency (exceeding 50%). This promising technology addresses the need for both high thrust and specific impulse in deep space exploration, making it a key candidate for future high-power propulsion solutions.[2–5]

Despite the excellent performance of electric propulsion, the lifespan of the cathode is a key factor that limits the overall lifespan of electric thrusters.[6–8] The working principle of MPDTs involves the acceleration of plasma through Lorentz forces generated by the interaction between an electric arc and a magnetic field.[9–11] The performance of the thruster is positively correlated with the current magnitude. For MPDTs operating at power levels of hundreds of kW, the cathode current typically ranges between 500 A and 1000 A, which presents significant challenges for cathode longevity. Cathode erosion has long been a major focus in the study of arc plasma torches. Optical techniques are frequently employed by researchers for the accurate measurement of high-temperature objects in experimental studies.[12–15] J. Haidar developed an innovative two-wavelength pyrometry method for accurately measuring the surface temperature of pure and thoriated tungsten cathodes in high-current free-burning arcs. This approach involves measuring the total thermal radiation flux emitted from both the cathode and the surrounding plasma. To isolate the cathode's temperature, the plasma component is subtracted using a modified Abel-inversion transformation, ensuring that the thermal radiation originating from the plasma does not skew the results. This method offers a precise technique for characterizing cathode surface temperatures, crucial for understanding the thermal dynamics in high-current arc systems.[16] Xin Zhou investigated the arc-cathode erosion of both pure tungsten and 2% thoriated tungsten cathodes. The study involved measuring the cathode temperature distributions with high spatial resolution using an optical multichannel analyzer spectrometer system. This study provides an in-depth and detailed investigation into the erosion mechanisms of the cathode.[17] Zongju Yang conducted a multispectral analysis to accurately measure the true temperature distribution of the surface temperature field of pulsed vacuum arc cathode ma-

[†]Corresponding author. E-mail: 18510489511@163.com

© 2025 Chinese Physical Society and IOP Publishing Ltd. All rights, including for text and data mining, AI training, and similar technologies, are reserved.

terials under varying discharge currents. This approach involved utilizing multiple wavelengths of light to capture the thermal radiation emitted from the cathode, enabling a precise determination of its surface temperature across different operating conditions. The findings from this research provide critical insights into the thermal dynamics and performance characteristics of cathode materials in pulsed vacuum arc applications, which are essential for optimizing their design and enhancing their operational efficiency.[18] However, research on cathode erosion in hundreds of kW MPDTs under strong magnetic fields is still relatively limited. Due to the compact size of ion source cathodes, achieving high temporal and spatial resolution for temperature measurements poses significant challenges, particularly in the presence of the plume region. As a result, non-contact optical measurement methods have gained popularity in the study of magnetic plasma. For example, C. A. Boorghi *et al.* utilized color CCD cameras to observe changes in plasma structure.[19] Meanwhile, Simmons *et al.* successfully measured the temperature and non-uniformity of a thermionic cathode by employing a CCD camera based on radiation temperature measurements. This innovative approach has provided a valuable experimental method for analyzing cathode surface temperatures.[20]

In this study, a single CCD camera equipped with a specialized wavelength filter was employed to capture the temperature distribution of the cathode surface, effectively mitigating the interference from arc light. The temperature of the cathode in a MPDT operating at a power level of 15 kW was measured under specific operating conditions, which included a current of 240 A, a voltage of 65 V, an argon flow rate of 50 mg/s, and a magnetic field strength of 0.1 T. The cathode utilized in this thruster was constructed from lanthanum tungsten.

2. Testing system

2.1. System composition

The configuration of the high-power MPDT vacuum ignition test system is illustrated in Fig. 1, consisting of five primary subsystems: the vacuum system, power source system, propellant supply system, water-cooling system, and target thrust measurement system. The vacuum system establishes the necessary environment for thruster ignition, maintaining an ultimate vacuum pressure of 10^{-4} Pa. The power source system supplies ignition, excitation, and anode power to the thruster while monitoring electrical parameters, including steady-state discharge voltage and current, excitation coil voltage and current, as well as arc initiation voltage and current. The propellant supply system delivers argon to the thruster cathode at a flow rate of 0–150 mg/s. The water-cooling system circulates deionized water to the anode, cathode, and excitation coils for cooling, while also monitoring temperature data from six inlet and outlet pipes, as well as the anode shell and cathode components.

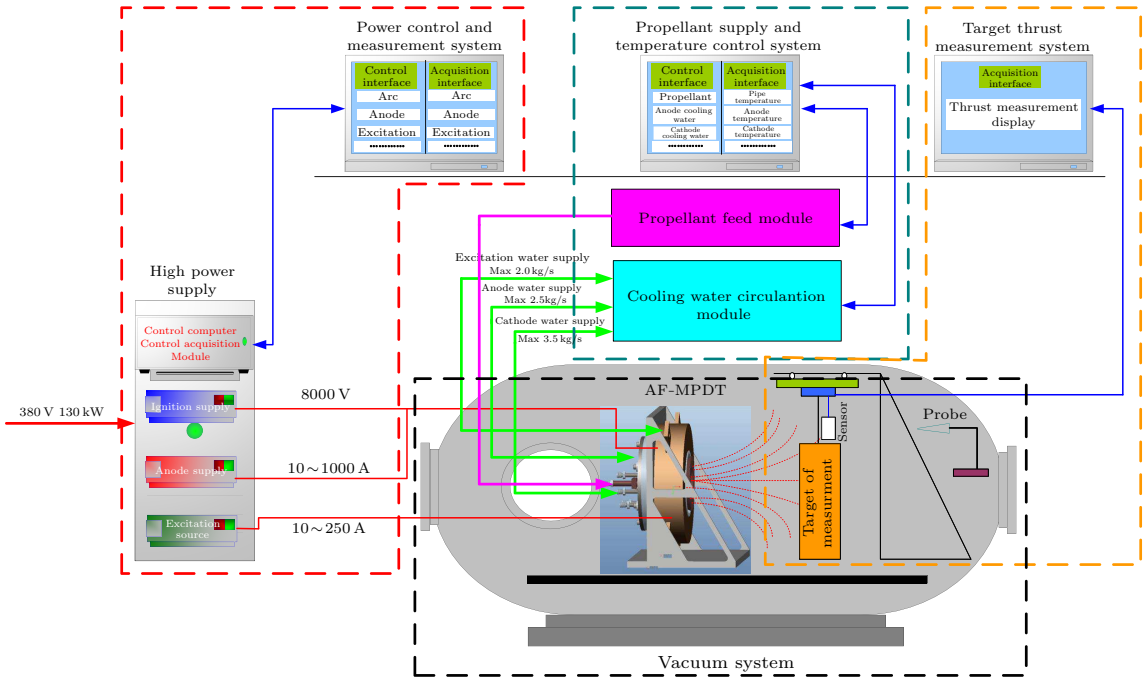


Fig. 1. Composition diagram of ignition test system for high-power MPDT.

2.2. Main experimental equipment

The high-power electric propulsion vacuum test system is primarily composed of large-scale vacuum equipment, including a large vacuum tank, three cryogenic vacuum pump systems with ultra-high pumping speeds, six xenon vacuum pump systems, two high-power molecular pump systems,

high-power vacuum root pump systems, a large-scale ultra-high pumping speed central control system, and fully elastic directional thermal deformation compensation devices. To maintain the vacuum environment necessary for high-power MPDT ignition, ranging from 10^{-1} Pa to 10^{-4} Pa, all three cryogenic pumps can be activated simultaneously. Additionally, the vacuum system is equipped with a beam protection system to mitigate the sputtering of xenon particles during ignition. This beam protection system features a heat sink-like structure, with all components made of titanium, as shown in Fig. 2.



Fig. 2. View of large vacuum system and beam protection plate.

The power source system provides high-voltage ignition pulses, anode power, and excitation power for the startup of the electromagnetic thruster, while also ensuring its stable operation and thrust generation. This system utilizes advanced switching power supply technology based on high-frequency inverters and is equipped with a high-frequency trigger system. Operating in constant current control mode, it includes features for setting power supply states, input/output index testing, and fault protection mechanisms against issues such as water shortages, overvoltage, overcurrent, and overheating. The power source system consists of an arc-starting power supply, anode power supply, excitation power supply, internal controller, switch panel, remote controller, testing tools, equipment cabinet, and cooling system. The thruster power source provides a direct current of up to 1000 A and a max discharge voltage of 250 V. The coil power source provides a direct current of up to 250 A. The discharge voltage and the thrust signal are acquired by the GEN2i data acquisition of HBM.

2.3. MPDT

The configuration of the MPDT used in this test is illustrated in Fig. 3. It primarily consists of five components: the cathode, anode, insulation structure, water-cooled structure, and superconducting magnet.

The primary structure of the MPDT consists of a magnet, cathode, and anode, along with additional components, such as insulation and sealing structures. To achieve a compact overall design while ensuring structural integrity and ease of assembly, efforts are made to minimize both axial and radial dimensions of the components. TC4 titanium alloy is used for the cathode and anode connectors, while boron nitride ceramic serves as the insulating material in high-temperature regions. The cylindrical anode features a water-cooling structure to dissipate heat from its surface, with inner and outer diameters of 60 mm and 165 mm, respectively, and a length of 30 mm. Propellant is injected solely through the cathode, which is made of lanthanum tungsten, measuring 10 mm in length (within the discharge chamber) and 24 mm in diameter. The cathode includes 24 channels, each with a diameter of 3 mm, and is housed within a water-cooled copper structure.

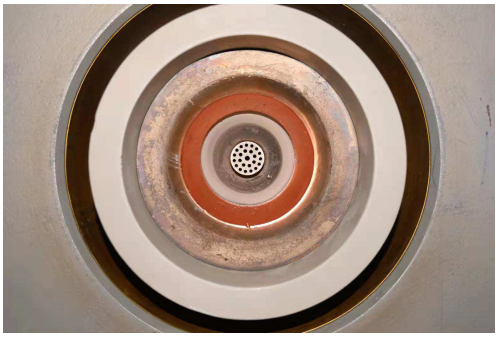


Fig. 3. View of low temperature superconducting MPDT.

3. Measuring method

Various methods exist for measuring the surface temperature of objects, with the radiation method being widely employed in experiments involving extremely high-temperature surfaces. This method is grounded in the principles of blackbody radiation law. Temperature measurement via radiation can primarily be categorized into monochromatic and colorimetric methods. Given the large size of the vacuum chamber utilized in this experiment and the significant distance between the calcium fluoride window and the MPDT cathode, the monochromatic temperature measurement method, which employs a single camera, emerged as the optimal choice for this study. Figure 4 is the schematic diagram of the MPDT optical diagnosis experimental test equipment.

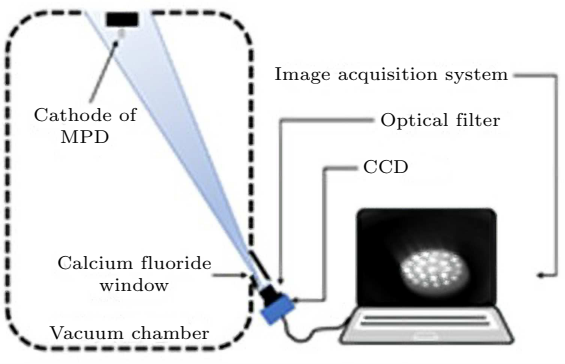


Fig. 4. Schematic diagram of MPDT optical diagnosis experimental test equipment.

A CCD camera (IMI-147FT) equipped with a telephoto lens (80–200 mm) and a filter centered at a wavelength of 890 nm is installed in a window on the vacuum chamber wall. During the experiment, the lens's focal circle is adjusted, and the camera's exposure time is optimized to capture a clear image of the cathode within the image acquisition system. Subsequent image processing allows for the extraction of temperature field information of the discharge electrode. Camera parameters in the test: 1 μs, focal length 200, aperture 22, effective focusing distance 4.6 m, lens 80–200. The basic parameters of the camera are SN:477, whiteness coefficient 490, sharpness coefficient 550, linearity coefficient 10 and gain 0. Monochromatic thermometry employs the relationship between the radiation energy at a specific wavelength and temperature to determine the temperature of the object. According to Planck's law, for a gray body, the spectral radiation capacity at a single wavelength is related to temperature by the following equation:

$$M(\lambda, T) = \frac{C_1}{\lambda^5} \frac{\varepsilon}{e^{\frac{C_2}{\lambda T}} - 1}, \tag{1}$$

where $C_1 = 3.742 \times 10^{-16}$ W·m^2 and $C_2 = 1.439 \times 10^{-2}$ m·K are Planck radiation constants and surface emissivity. In fact, the monochromatic temperature measurement method relies on the relationship between total radiant energy and temperature within a specified narrow wavelength band. Therefore, the integral of Eq. (1) over this band establishes the connection between total radiant energy and temperature.

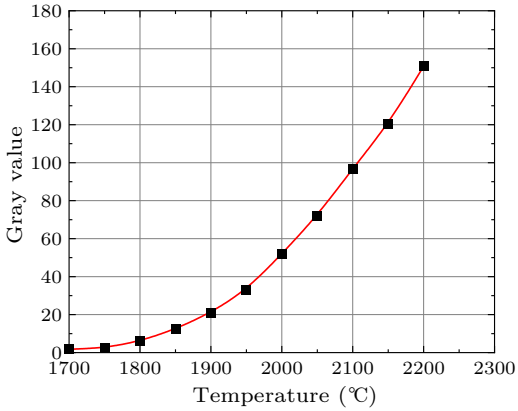


Fig. 5. Calibration curve of the relationship between CCD output grayscale and temperature in this experiment.

In this experiment, establishing a definitive link between the response metrics of the camera, specifically the pixel grayscale value, and the corresponding temperatures, is crucial for determining the cathode temperature from radiation intensity. Utilizing the program-controlled tubular furnace, the cathode material was incrementally heated to various temperatures. The filtration and camera settings were meticulously aligned with those prescribed in the MPDT optical diagnosis experiment. Subsequently, the grayscale values recorded by the camera at different temperatures were subjected to a fitting process, resulting in a fifth-order polynomial curve that encapsulates the relationship between temperature and grayscale level, as illustrated in Fig. 5. This curve now serves as a foundational database for the post-processing phase of temperature measurement.

4. Experimental results

When using a single camera for cathode temperature measurement, susceptibility to interference from arc light and reflections off adjacent metal surfaces becomes significant. As shown in Fig. 6, grayscale images captured at arc initiation, stabilization, and flameout stages are processed with pseudo-color enhancement. The MPDT operates under parameters of a 0.1 T magnetic field, 240 A current, and 65 V voltage without a filter.

During the initial phase, characterized by intense arc light, the cathode is completely obscured, making it challenging for single-camera imaging to accurately differentiate radiation intensity from the arc and the cathode. While the arc light diminishes during stable operation, the residual plume continues to interfere with precise assessment of the cathode's surface radiation intensity. Therefore, selecting an appropriate filter is essential to improve the accuracy and reliability of this testing methodology.

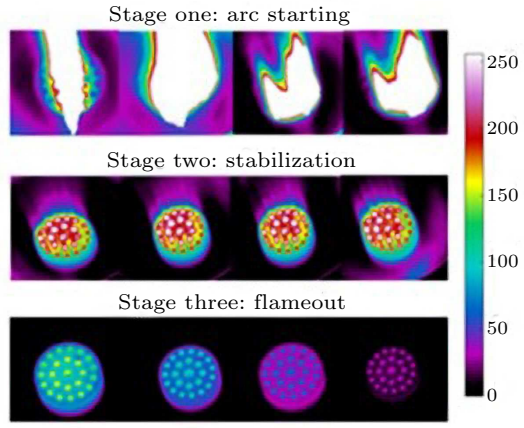


Fig. 6. Changes in the working state of the cathode taken by a single CCD camera without a filter.

To mitigate interference from arc light, it is crucial to carefully select a spectral band with minimal radiation for accurate cathode temperature detection. Due to the linear emission spectrum characteristics of argon plasma, identifying an appropriate band filter is a relatively straightforward process. In this experiment, the radiation spectra of argon (Ar) and its ions primarily appear in the plasma plume, encompassing Ar III spectra from 320 nm to 350 nm, Ar II spectra from 350 nm to 500 nm, and Ar I spectra from 690 nm to 900 nm. As shown in Fig. 7, the emission spectral intensity distribution near the cathode is illustrated across various wavelengths.

Wavelengths exceeding 850 nm are observed to exhibit near-zero spectral intensity. Based on this observation, a filter with a central wavelength of 890 nm and a half-width of 20 nm is selected, effectively eliminating arc light interference during temperature measurements.

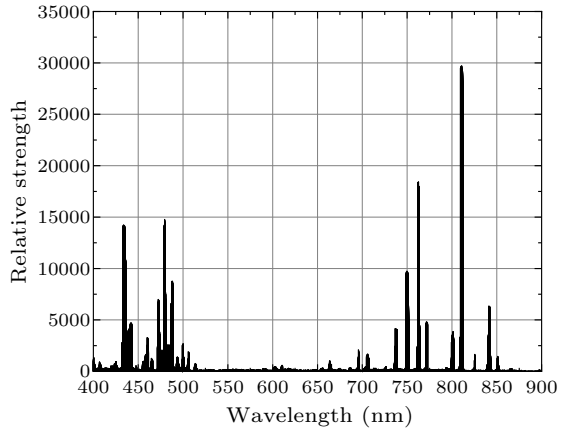


Fig. 7. Intensity distribution of magnetic plasma emission spectra at different wavelengths.

Figure 8 illustrates the fluctuations in radiation intensity across the cathode surface during the discharge process, following the installation of the filter. As the plasma plume reaches a stable state, a clear distribution of radiation intensity becomes evident on the cathode surface. This monochromatic temperature measurement method functions effectively without imposing additional constraints regarding interference from external radiation sources.

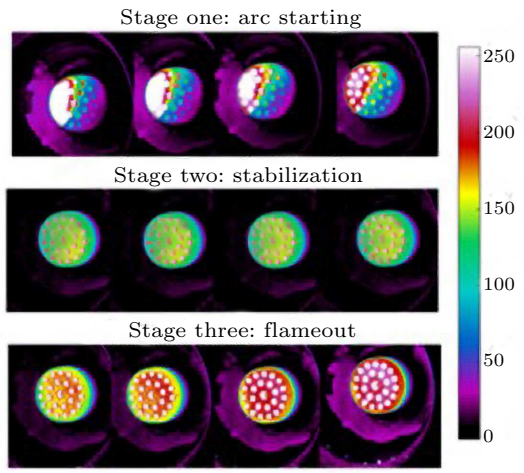


Fig. 8. Using a filter with a central wavelength of 890 nm.

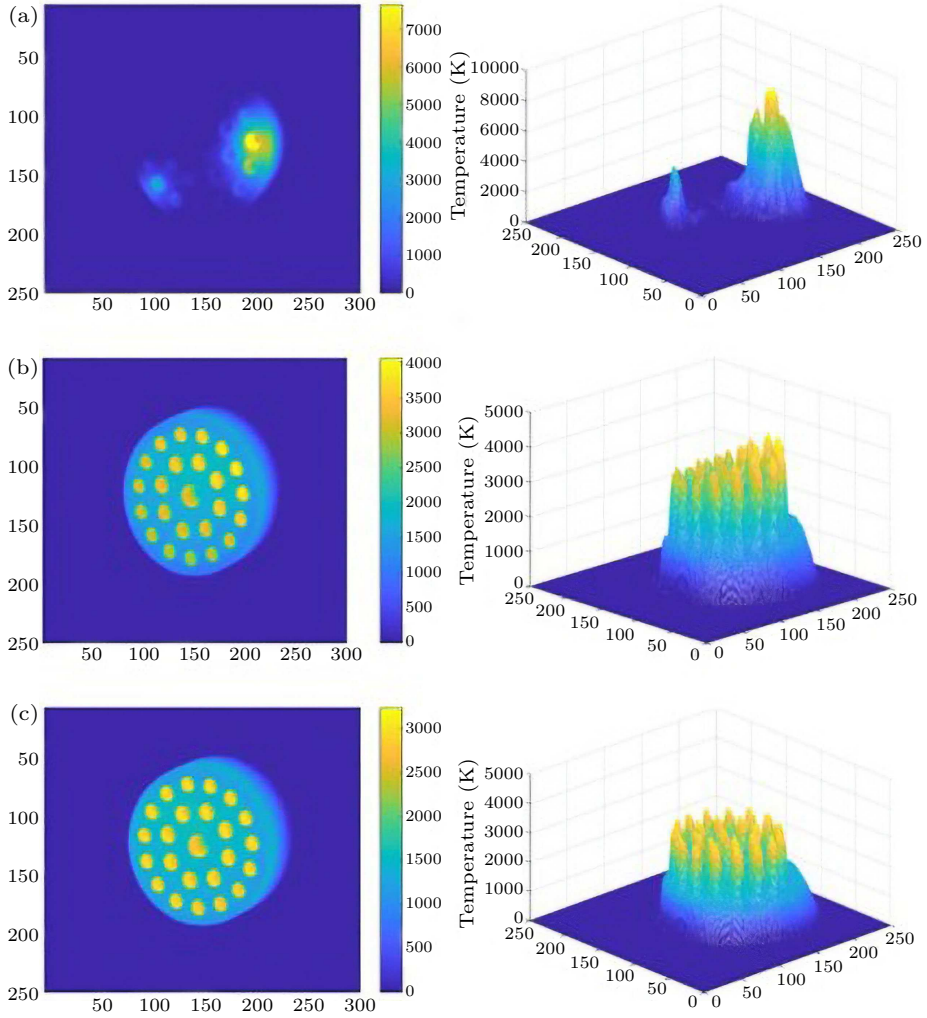


Fig. 9. Cathode surface and axial temperature distribution at (a) $t = 2.0$ s, (b) $t = 15.7$ s and (c) $t = 20.0$ s.

The temperature distribution of the cathode surface and along the axial direction at different times can be determined using the output grayscale values and temperature calibration curves, as shown in Fig. 9. During the discharge initiation phase at $t = 2.0$ s, two small apertures appear in the upper right and lower right regions of the cathode, where surface discharge gradually converges. As time progresses to $t = 15.7$ s, the intense radiation initially observed in the upper right quadrant expands into adjacent regions, eventually enveloping the entire cathode surface. Concurrently, the surface temperature reaches thermal equilibrium. By $t = 20.0$ s, a slight reduction in surface temperature occurs, accompanied by a slight increase in axial temperature, marking the point at which both surface and axial temperatures achieve thermal equilibrium. Additionally, a distinct temperature gradient forms along the flank of the cathode. As the axial distance increases, the temperature drops rapidly, with the high-temperature zone confined to a depth of only 1 cm at the end.

Due to constraints imposed by the plume and the viewing angle within the cathode orifice, the temperature post-processing focused exclusively on the distribution of temperature on the outer surface. Figure 10 depicts the temperature distribution of the cathode surface in a stable state. Notably, the vicinity of the spray orifice registers elevated temperatures, which is a direct cause of cathode ablation damage. As shown in Fig. 10, the highest temperature on the cathode is concentrated on the inner wall of the small hole, where it reaches approximately 3000 °C. This is likely due to the higher plasma density inside the hole, resulting in more intense particle bombardment and enhanced convective heat transfer to the cathode in this region. The temperature across the entire cathode end face is primarily between 2200 °C and 2400 °C, while the outer regions, where the plasma density is lower, maintain a temperature around 2000 °C.

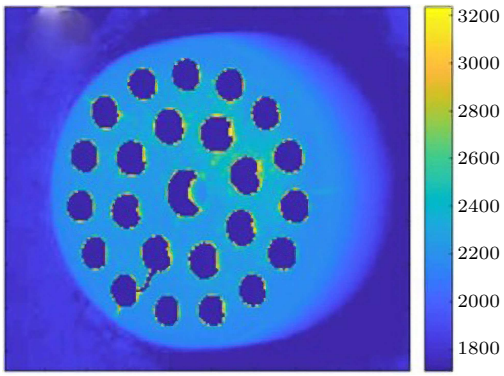


Fig. 10. Temperature distribution on the cathode end face.

Figure 11 illustrates the temporal trajectory of the average temperature at the cathode end face. The cathode experiences continuous heating during the arc initiation phase, reaching high temperatures within just 15 s. Subsequently, temperature increments proceed gradually, stabilizing between 2200 °C and 2400 °C during sustained operation. When the thruster is turned off, the temperature drops rapidly, indicating a strong heat transfer capability from the end face of the cathode to its interior.

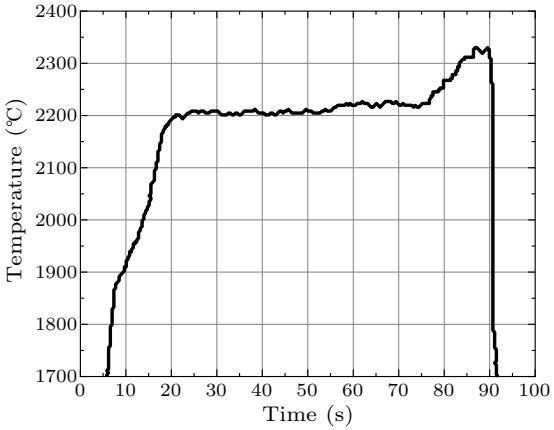


Fig. 11. Change curve of average temperature of cathode end face with time.

5. Conclusion

This study successfully elucidates the temperature distribution of the cathode surface and along the axial direction over time, utilizing output grayscale values in conjunction with temperature calibration curves. Observations during the discharge initiation phase reveal the emergence of two small apertures on the cathode, indicating the onset of surface discharge. As time progresses, the intense radiation initially localized in the upper right quadrant expands, eventually encompassing the entire cathode surface, while the temperature reaches equilibrium.

By the end of the 20-second observation period, both surface and axial temperatures reach thermal equilibrium. A pronounced temperature gradient forms along the flank of the cathode, characterized by a rapid temperature drop over an axial distance confined to approximately 1 cm.

The investigation reveals that elevated temperatures near the spray orifice significantly contribute to cathode ablation, emphasizing the critical role of thermal behavior in ensuring cathode longevity. Temporal analysis of the average temperature at the cathode end face shows rapid heating during the arc initiation phase, with temperatures reaching high levels within 15 s. This is followed by a stabilization phase, during which temperatures range from 2200 °C to 2400 °C under steady-state operation. Upon shutdown, the rapid temperature drop highlights efficient heat transfer from the end face to the cathode's interior.

These findings provide valuable insights into the thermal dynamics of MPDT cathodes, emphasizing the need for further research into mitigating thermal stresses and enhancing

the operational lifespan of cathodes in high-power applications.

References

[1] Li X K, Che B X, Cheng M S, Guo D W, Wang M G and Yang Y T 2020 *Chin. Phys. B* **29** 115201

[2] Albertoni R, Paganucci F, Rossetti P and Andrenucci M 2013 *Journal of Propulsion and Power* **29** 1138

[3] Boxberger A and Herdrich G 2017 *The 35th International Electric Propulsion Conference* (Georgia Institute of Technology, Atlanta, Georgia, USA: Electric Rocket Propulsion Society) p. 339

[4] Voronov A S, Troitskiy A A, Egorov I D, Samoilenkov S V and Vavilov A P 2020 *J. Phys.: Conf. Series* **1686** 012023

[5] Zheng J, Liu H, Song Y, Zhou C, Li Y, Li M, Tang H, Wang G, Cong Y, Wang B, Wang Y, Wu P, Qu T, Zhu X, Zhu L, Liu F, Cheng Y and Zhao B 2021 *Sci. Rep.* **11** 22336

[6] Albertoni R 2012 *Cathode Processes in MPD Thrusters* PhD Thesis (University of Pisa Pisa)

[7] Zhang Z, Ling W Y L, Tang H, Cao J, Liu X and Wang N 2019 *Rev. Mod. Plasma Phys.* **3** 5

[8] He L L, He F and Ouyang J T 2024 *Chin. Phys. B* **33** 035203

[9] Coletti M 2007 *The 43rd AIAA/ASME/SAE/ASEE Joint Propulsion Conference & Exhibit Joint Propulsion Conferences* (Cincinnati, OH: American Institute of Aeronautics and Astronautics) p. 5284

[10] Coletti M 2012 *Acta Astronautica* **81** 667

[11] Coogan W and Choueiri E 2017 *53rd AIAA/SAE/ASEE Joint Propulsion Conference* (Atlanta, GA: American Institute of Aeronautics and Astronautics) p. 4723

[12] Xin C Y, Du X P, Guo F Q and Sheng S L 2019 *Spectroscopy and Spectral Analysis* **39** 679

[13] Hartmann J 2009 *Phys. Rep.* **469** 205

[14] McMillan J L, Greenen A, Bond W, Hayes M, Simpson R, Sutton G, Machin G, Jowsey J and Adamska A 2019 *Measurement* **132** 207

[15] Teixeira R N and Machin G 2017 *Int. J. Thermophys* **38** 80

[16] Haidar J and Farmer A J D 1993 *Rev. Sci. Instrum.* **64** 542

[17] Zhou X, Ding B and Heberlein J 1996 *IEEE Transactions on Components, Packaging, and Manufacturing Technology: Part A* **19** 320

[18] Yang Z, Dai J and Zhang J 2022 *Measurement Science and Technology* **33** 055501

[19] Borghi C, Carraro M, Cristofolini A, Ghidini R and Paganucci F 2003 *34th AIAA Plasmadynamics and Lasers Conference Fluid Dynamics and Co-located Conferences* (American Institute of Aeronautics and Astronautics)

[20] Simmons D F, Fortgang C M and Holtkamp D B 2005 *Rev. Sci. Instrum.* **76** 044901